Applied Surface Science 421 (2017) 593–600

Contents lists available at ScienceDirect

Applied Surface Science

journal homepage: www.elsevier.com/locate/apsusc

Optical response of gold hemispheroidal lattices on transparent substrates

Morten Kildemo[a,*], Jean-Philippe Banon[a], Alexandre Baron[b], Brage B. Svendsen[a], Thomas Brakstad[a], Ingve Simonsen[a,c]

[a] Department of Physics, NTNU Norwegian University of Science and Technology, NO-7491 Trondheim, Norway
[b] CNRS, Centre de Recherche Paul Pascal, UPR 8641 115 Avenue Schweitzer, 33600 Pessac, France
[c] Surface du Verre et Interfaces, UMR 125 CNRS/Saint-Gobain, F-93303 Aubervilliers, France

ARTICLE INFO

Article history:
Received 30 July 2016
Received in revised form 2 February 2017
Accepted 2 February 2017
Available online 20 February 2017

Keywords:
Mueller Matrix Ellipsometry
Plasmonics
Optical properties
Polarimetry

ABSTRACT

Square arrays of gold (Au) hemispheroids deposited on a UV-transparent glass substrate reveal a rich optical response when investigated by spectroscopic Mueller Matrix Ellipsometry. Two samples were studied; the first consisted of hemispheroids of parallel radius of 58 nm and height 30 nm with lattice constant 210 nm; the corresponding parameters for the second sample were 38 nm, 20 nm and 125 nm, respectively. By a full azimuthal rotation of the samples, we observe all the Rayleigh anomalies corresponding to grazing diffracted waves, with strong resonances for co-polarization scattered light near the high symmetry points and cross-polarization scattered light around the Localized Surface Plasmon Resonance. Polarization-conversion becomes particularly important at grazing incidence, and the cross-polarization follows the Rayleigh lines. The optical response (neglecting polarization conversion) is modelled in the quasi-static approximation using the so-called Bedeaux-Vlieger formalism, and the Finite Element Method using COMSOL. The direct inversion of the effective (substrate dependent) dielectric function is discussed.

1. Introduction

Mueller matrix ellipsometry is expected to play an important role in the characterization of plasmonic based devices, such as plasmonic metamaterials/metasurfaces [1,2], or composite nanoplasmonic devices with applications ranging from optoelectronics to biomedicine [3–5]. The fascinating properties of metamaterials can be exemplified by e.g. the negative refractive index [6] and its application to perfect lensing and subdiffraction imaging [7].

The metamaterials approach consists in determining effective electromagnetic parameters for an inhomogeneous periodic artificial material. As such, the metamaterials approach bridges the gap between low-frequency effective medium theory and the high frequency diffractive regime (therein photonic crystals) [8]. However, it is necessarily the combined response that will be observed by spectroscopy across a larger spectral range.

Here we study an apparently simple model system consisting of hemispheroidal Au particles organized in a square lattice on a UV-transparent flat glass substrate. The particle dimensions are such that the quasistatic approximation should be valid, at least for the longest wavelengths. This system was recently shown to have a rich optical response including polarization coupling around the Localized Surface Plasmon Resonance (LSPR), and around so-called Rayleigh anomalies (or Rayleigh lines) related to grazing diffracted waves just at the onset of diffracted orders [2].

Indeed, the importance of the polarization coupling can be directly observed in Mueller matrix spectroscopic studies with complete azimuthal sample rotation of inherently anisotropic systems, such as self-assembled Ag or Au particles along the ripples of a nanopatterned substrate [9–11], meta-surfaces of U-shaped particles [12], slanted metallic pillars [13], and chiral structures [14].

In this paper, the regular lattices of idealized metallic hemispheroids supported by a flat dielectric substrate (here SiO_2) are modelled by the Bedeaux-Vlieger theory [15]. Since this theory does not account for cross-polarized scattered light, only a block-diagonal Mueller matrix can be obtained within this approach. In order to account for cross-polarized scattered light, and therefore obtaining non-vanishing off-diagonal elements of the Mueller matrix, more accurate and time consuming modelling approaches have to be used. One possibility is to perform the modelling on

* Corresponding author.
E-mail address: Morten.Kildemo@ntnu.no (M. Kildemo).

http://dx.doi.org/10.1016/j.apsusc.2017.02.008
0169-4332/

the basis of the reduced Rayleigh equation [16,17] which recently was shown to produce reliable results for the Mueller matrix elements [18]. Other approaches, often used in the metamaterials community, are the full wave solutions obtained by the Finite Element Method (FEM) and Finite Difference Time Domain (FDTD) simulations. In this work we will present results obtained by FEM simulations.

2. Experimental

The samples were produced by evaporating a thin film of Au onto a clean (and flat) UV-grade fused silica surface using an e-beam evaporator (Pfeiffer Vacuum Classic 500). The deposited film thicknesses were 40 nm (Sample A) and 20 nm (Sample B). The resulting films were smooth but polycrystalline. The Au nano-structures on glass were produced by Focused Ion Beam (FIB)-milling using Ga ions (FEI Helios Dual-beam FIB). The two samples reported here were manufactured to make up Au hemispheroids distributed in a square pattern on a glass-surface, see Fig. 1(a); the lattice constants were $a = 210\,nm$ (Sample A) and $a = 125\,nm$ (Sample B). After the milling, the particles were found to be hemispheroids of lateral radius $R_{xy} = (58 \pm 4)$ nm (Sample A), and (38 ± 4) nm (Sample B), see Fig. 1(c). The heights of the particles (the perpendicular radii) were difficult to estimate accurately from the combination of AFM and SEM images. However, rough estimates are $R_z = 30\,nm$ for Sample A (<40 nm) and $R_z = 25\,nm$ for Sample B (with an expected uncertainty of several nanometers). Unfortunately, an over-etching into the substrate was observed for both samples, i.e. the Au particles are probably on top of a dielectric mound, as roughly sketched in Fig. 1(d). Both samples had an over-milling of at least 10 nm into the substrate.

The surface coverage for a square lattice of hemispheroidal particles is defined as $\Theta = \pi R_{xy}^2/a^2$, giving $\Theta_A = 0.20$ and $\Theta_B = 0.18$ for the coverage of Sample A and Sample B, respectively.

For the optical characterization of the samples, a variable angle multichannel dual rotating compensator Mueller matrix ellipsometer (RC2) from JA Woollam Company was used. Our instrument has a collimated 150 W Xe source and operates in the spectral range from 210 nm (5.9 eV) to 1700 nm (0.73 eV). As the FIB-milling is a time consuming process, the total milling area opened by FIB was limited to 240 μm × 240 μm. Focusing and collection lenses with a focal length of 20 mm and a Numerical Aperture of approximately 0.15, were applied, allowing a normal incidence spot size of smaller 100 μm. This spot size allowed us to study the full azimuthal rotation of the sample while ensuring that the spot-size remained within the 240 μm × 240 μm area. The spectroscopic Mueller matrix was measured for the polar incidence angles (with respect to surface normal) $\theta_0 = 45°$, 55° and 65°. Full azimuthal rotation of the sample around the sample normal (360°) in steps of 5° was performed for each polar angle of incidence in order to fully map any anisotropy in the optical response of the sample (see Brakstad et al. [2] for further details).

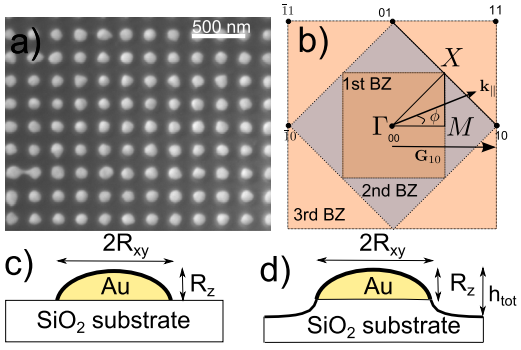

Fig. 1. (a) Real space Scanning Electron Microscopy (SEM) image of the particle array. (b) Schematic drawing of the 2-dimensional reciprocal lattice defining ϕ_0. (c) The ideal model consisting of a hemispheroidal Au particle on uv-transparent glass. (d) The presumed non-ideal model with the particles on a mound.

3. Results and discussion

3.1. Mueller matrix: LSPR, Rayleigh lines and polarization coupling

Fig. 2 presents an overview of the normalized Mueller matrix optical response, **m**, measured for Sample A as a function of the photon energy ($E = \hbar\omega$), for the specular direction $[(\theta_0, \phi_0) = (\theta_s, \phi_s)]$. A series of measurements were performed for a fixed polar angle of incidence $\theta_0 = 55°$, but different values of the azimuthal angle of incidence ϕ_0. The coordinate system is defined so that the value $\phi_0 = 0°$ represents a direction that coincides with one of the main axes of the square lattice. In Fig. 2 the (2×2) block diagonal elements of **m** are stacked as functions of the azimuthal angle of incidence (except m_{22}). The corresponding SEM image of Sample A and a schematic diagram of the reciprocal lattice are shown in Fig. 1(a) and (b), respectively, see also Figs. 1–3 in Brakstad et al. [2]. We observe from the diagonal elements of the Mueller matrix that a LSPR exists for a photon energy around 2.1 eV, which is here found to be slightly dispersive with azimuthal rotation angle ϕ_0, see also Ψ_{pp} and $\langle\varepsilon\rangle_{pp}$ in Ref. [2]. Furthermore, we observe polarization conversion around the LSPR that dependends on ϕ_0; this is seen from the off-block-diagonal elements (which are not stacked) in Fig. 2. We further observe that there are prominent features in both the block-diagonal elements (dips and peaks) and the off-block-diagonal elements (strong polarization conversion); these features are attributed to the Rayleigh anomalies [19] as previously described in detail in Brakstad et al. [2] and references therein.

In recent works [2,9,20,21] we have found it useful to present Mueller matrix data in terms of contour plots in polar coordinates as they clearly show their dependence on the rotation of the sample. In such plots, the polar coordinate corresponds to the azimuthal rotation angle (ϕ_0) and the radial coordinate represents the photon energy. Fig. 3 presents in this fashion the normalized Mueller matrix data of which the data-sets from Fig. 2 are subsets; the inner and outer circles in Fig. 3 correspond to 0.73 eV and 5.9 eV, respectively. Notice that for given azimuthal rotation angle (ϕ_0), a cut along the radial direction of the data-sets presented in Fig. 3 will result in curves for the same value of ϕ_0 that are similar to those in Fig. 2. Moreover, the data in Fig. 3 are organized such that $\phi_0 = \angle(\mathbf{k}_\parallel, \mathbf{G}_\parallel^{(10)})$, where the component of the incident wave vector parallel to the surface of the substrate is ($|\mathbf{k}| = k = n_0\omega/c$)

$$\mathbf{k}_\parallel = k \sin\theta_0(\cos\phi_0, \sin\phi_0, 0), \tag{1}$$

and the reciprocal lattice vector is defined as

$$\mathbf{G}_\parallel^{(\mathbf{l})} = l_1\mathbf{b_1} + l_2\mathbf{b_2} = G_\parallel^{(\mathbf{l})}(\cos\phi_{\mathbf{l}}, \sin\phi_{\mathbf{l}}, 0), \tag{2}$$

where l_1 and l_2 are integers and $G_\parallel^{(\mathbf{l})} = |\mathbf{G}_\parallel^{(\mathbf{l})}|$. In writing Eq. (2) we have introduced the primitive translation vectors of the reciprocal lattice $\mathbf{b}_1$ and $\mathbf{b}_2$ ($|\mathbf{b}_{1,2}| = 2\pi/a$), and defined the vector $\mathbf{l} = (l_1, l_2)$ (see Ref. [2] for further details).

It is observed from Fig. 3 that the Mueller matrix of Sample A is nearly block-diagonal for photon energies up till about 3 eV, and the same was found also for Sample B (results not shown). The LSPR is now observed as the nearly circular features around 2.1 eV in all the block diagonal elements presented in Fig. 3. The Rayleigh lines observed in e.g. the m_{12} element, now make up a set of features that resembles the first and second Brillouin zone (BZ), see Fig. 1(b).

Brakstad et al. [2] described thoroughly the main features of these Rayleigh lines [19]. In particular, in this work, a compact

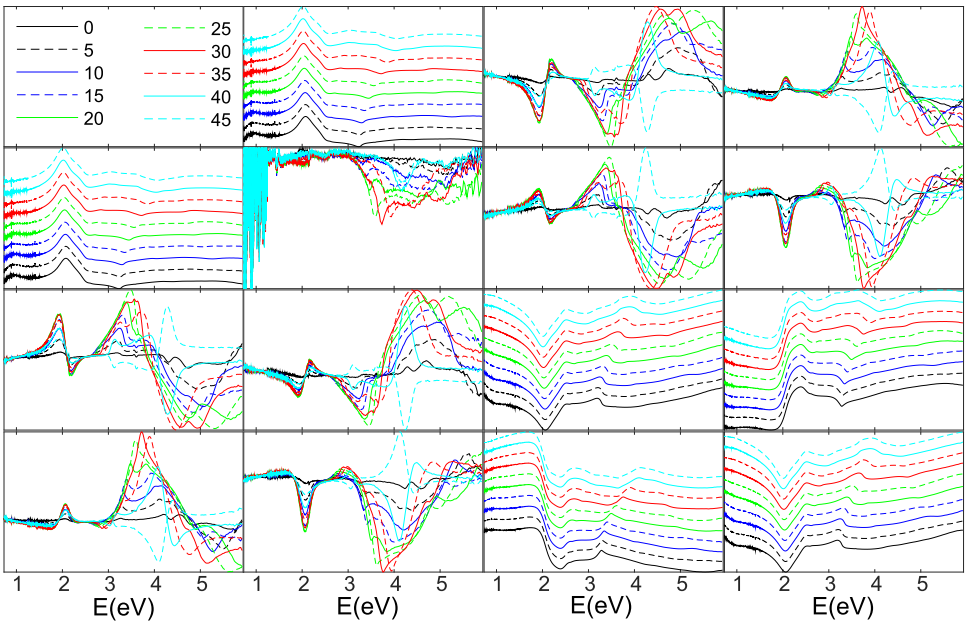

Fig. 2. Overview of the experimental normalized Mueller matrix elements for Sample A as functions of photon energy. The polar angle of incidence was $\theta_0 = 55^\circ$ and the azimuthal angle of incidence ϕ_0 was varied from 0° to 45° in steps of 5°. The measurements were done in the specular direction, i.e. $(\theta_s, \phi_s) = (\theta_0, \phi_0)$. The (2×2) block diagonals elements are stacked (except the m_{22} element), that is, a constant offset was added to each data set for reasons of clarity. The vertical limits for the off-diagonal elements are $m_{13} = [-0.103, 0.117]$, $m_{14} = [-0.079, 0.116]$, $m_{23} = [-0.097, 0.067]$, $m_{24} = [-0.148, 0.082]$. Similarly, $m_{31} = [-0.122, 0.102]$, $m_{32} = [-0.062, 0.098]$, $m_{41} = [-0.0696, 0.116]$, $m_{42} = [-0.149, 0.081]$, while $m_{22} = [0.96, 1]$. See the colorbars in Fig. 3 for the vertical limits for all elements and all azimuthal orientations. (For interpretation of the references to color in this figure legend, the reader is referred to the web version of this article.)

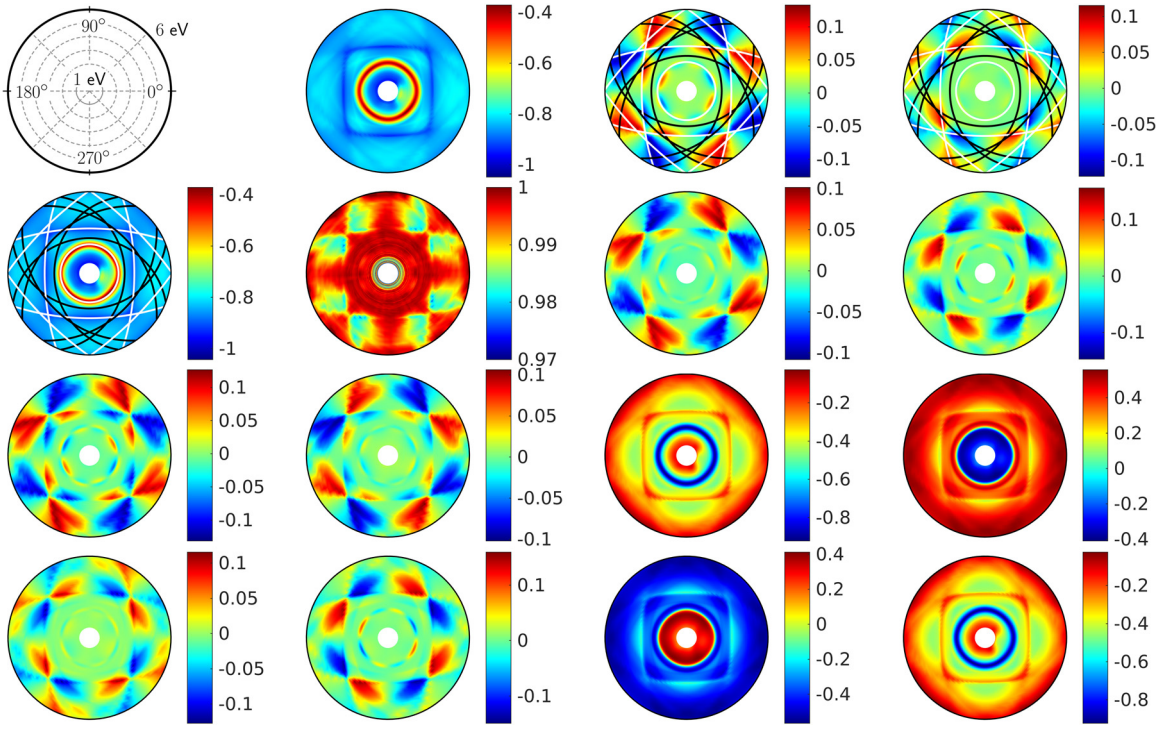

Fig. 3. Contour plots of the elements of the experimental normalized Mueller matrix **m** for the Sample A, measured for $\theta_0 = \theta_s = 55^\circ$ and $\phi_0 = \phi_s$ (where θ_s and ϕ_s denote the polar and azimuthal angles of scattering). The photon energy and the azimuthal rotation angle (ϕ_0) of the incident light represent the radius and the angle in these polar plots, respectively. The inner circles in the plots correspond to the photon energy 0.73 eV, while the outer correspond to 5.90 eV. The Rayleigh-lines for the first BZ (upright semi-square), the 2nd BZ (tilted semi-square) in air (white lines), and in the glass substrate (black lines) have been superimposed on the m_{21} element. In the m_{13} and m_{14} elements, the extended Rayleigh-lines for air (white lines) and glass (black lines) that were calculated for a 90° symmetry are superimposed, in addition to the LSPR resonance at 2.1 eV (white circles) as estimated from the quasi-static approximation. The circles in the schematic inset, replacing the m_{11} element (that is trivially one), correspond to the photon energy of the incident light from 1 eV (thick inner line) to 6 eV (thick outer line) in steps of 1 eV, while 0, 45, 90, etc. denote the azimuthal rotation angle (ϕ_0) in degrees. (For interpretation of the references to color in this figure legend, the reader is referred to the web version of this article.)

expression for the Rayleigh line condition was rederived, and it reads [2]

$$k^2 - \frac{2k\sin\theta_0 G_{\parallel}^{(\mathbf{I})}\cos(\phi_{\mathbf{I}} - \phi_0)}{n_i^2 - \sin^2\theta_0} - \frac{\left(G_{\parallel}^{(\mathbf{I})}\right)^2}{n_i^2 - \sin^2\theta_0} = 0, \tag{3}$$

where n_i denotes the refractive index of either the ambient (air) or the substrate (SiO_2). The form in Eq. (3) is extremely useful, as it allows to either solve for the Rayleigh lines, the lattice constants or even the refractive index of the substrate.

The Rayleigh lines calculated from Eq. (3) are shown in Fig. 3 as black lines for the substrate and white lines for air, and they describe the main features of the block-diagonal elements of the Mueller matrix. The polarization conversion is now clearly observed from Fig. 3 as regular dots around the LSPR (with maxima for incidence midway between $\Gamma - X$ and $\Gamma - M$). It is also clearly observed from the results presented in Fig. 3 that the polarization conversion is found around the Rayleigh lines [2], i.e. around the black (substrate) and white (air) Rayleigh lines drawn in the m_{13} and m_{14} elements.

We speculate that the polarization coupling around the LSPR is a result of spatial dispersion [22,12], while the polarization coupling around the Rayleigh lines is a result of a modification of the effective polarizability tensor as a result of the grazing diffracted waves. In the remaining part of this paper we will focus on modelling the approximately near block diagonal response below the Rayleigh lines, in particular using the Bedeaux-Vlieger formalism, and full wave COMSOL simulations.

3.2. Bedeaux-Vlieger model

Over several decades, starting in the 1970s, Bedeaux and Vlieger developed an approach to the calculation of the optical properties of thin island films (or rough surfaces) that is based on the use of effective boundary conditions [15,23–25,1,26]. The Bedeaux-Vlieger (BV) model introduces so-called surface suceptibilities, related to particle polarizabilities, that modifies the well-known Fresnel amplitudes of a flat surface to account for the presence of the island film (or surface roughness) [see Eqs. (4) and (7)]. When no particles (islands) are present at the flat surface of the substrate, the surface suceptibilities vanish and the modified Fresnel amplitudes reduce to the classic and well-known Fresnel amplitudes; in this sense the surface suceptibilities encode the effects of the presence of the island film. Within the BV model, the polarizability of a particle is calculated within the quasi-static approximation by means of adapting a multipole expansion of the scalar electric potential [15,23,24,27]. This is achieved by first calculating, to a high multipole order, the interaction between a single particle and the substrate by the use method of images [27]. Next, the single-particle polarizability is corrected for particle-particle interactions by assuming that this can be done adequately by only including dipolar or quadrupolar interactions. That is, the particle-particle interaction is included only to a low multipolar order which is expected to be a good approximation in the low particle coverage limit. In this way, the particle polarizabilities are calculated within the BV model, and from them, the surface suceptibilities and, therefore, the optical response can be calculated. For a more detailed discussion of the BV model the interested reader is referred to Refs. [15,23,24]. It should be mentioned that the BV formalism is implemented in the (open source) software GranFilm developed by Simonsen and Lazzari [25]. The advantage of the BV formalism is that it results in a fast calculation (fraction of seconds) of the full spectrum.

The BV model introduces two types of surface susceptibilities that are either *parallel* or *perpendicular* to the surface of the substrate; in accordance with Ref. [15], we will in the following denote them $\gamma(\omega)$ and $\beta(\omega)$, respectively.

When light of s polarization is incident from an ambient medium of refractive index n_0, onto an island film supported by the flat surface of a substrate that has refractive index n_2, the BV model predicts that the reflection amplitude should equal [15,25]:

$$r_{012s}(\omega) = \frac{n_0\cos\theta_0 - n_2\cos\theta_2 + i\frac{\omega}{c}\gamma(\omega)}{n_0\cos\theta_0 + n_2\cos\theta_2 - i\frac{\omega}{c}\gamma(\omega)}. \tag{4}$$

Here, θ_0 and θ_2 are the polar angles of incidence and transmission, respectively, and they are measured positive from the normal to the mean surface. It is convenient to rewrite Eq. (4) in the alternative form

$$r_{012s}(\omega) = \frac{r_{02s}(\omega) + i\frac{\omega}{c}\frac{\gamma(\omega)}{\eta_s}}{1 - i\frac{\omega}{c}\frac{\gamma(\omega)}{\eta_s}}, \tag{5}$$

with $\eta_s = n_0\cos\theta_0 + n_2\cos\theta_2$, so that the Fresnel reflection amplitude for the ambient-substrate system, $r_{02s}(\omega)$, enters explicitly; this latter quantity is defined by the expression obtained by putting $\gamma = 0$ in Eq. (4).

Similarly, for p-polarized incident light the reflection amplitude of an island film is expressed in the BV model as [15,25]:

$$r_{012p}(\omega) = \frac{\kappa_-(\omega) - i\frac{\omega}{c}\left[\gamma\cos\theta_0\cos\theta_2 - n_0 n_2\varepsilon_0\beta\sin^2\theta_0\right]}{\kappa_+(\omega) - i\frac{\omega}{c}\left[\gamma\cos\theta_0\cos\theta_2 + n_0 n_2\varepsilon_0\beta\sin^2\theta_0\right]} \tag{6a}$$

where

$$\kappa_\pm(\omega) = (n_2\cos\theta_0 \pm n_0\cos\theta_2)\left(1 - \frac{1}{4}\frac{\omega^2}{c^2}\gamma\beta\varepsilon_0\sin^2\theta_0\right). \tag{6b}$$

For reasons of a more compact presentation, we have in Eq. (6) not indicated explicitly the frequency dependence of the surface susceptibilities. Neglecting terms of second or higher order in the surface susceptibilities allow us to write Eq. (6a) approximately as

$$r_{012p}(\omega) \approx \frac{r_{02p}(\omega) - i\frac{\omega}{c}\frac{1}{\eta_p}\left[\gamma\cos\theta_0\cos\theta_2 - n_0 n_2\varepsilon_0\beta\sin^2\theta_0\right]}{1 - i\frac{\omega}{c}\frac{1}{\eta_p}\left[\gamma\cos\theta_0\cos\theta_2 + n_0 n_2\varepsilon_0\beta\sin^2\theta_0\right]}. \tag{7}$$

In writing Eq. (7) we have defined $\eta_p = n_2\cos\theta_0 + n_0\cos\theta_2$ and $r_{02p}(\omega)$ denotes the Fresnel reflection amplitude of the flat ambient-substrate surface for p-polarized illumination [27,28] and can be obtained by putting $\gamma = \beta = 0$ in Eq. (6).

Several parameters are needed to calculate the surface susceptibilities, $\gamma(\omega)$ and $\beta(\omega)$, in the approach of BV. In addition to the wavelength, angles of incidence (θ_0, ϕ_0), and refractive indices of the media involved, they are the *morphological parameters* of the hemispheroidal island film; the radii of the hemispherodal particles that are parallel (R_{xy}) and perpendicular (R_z) to the surface of the substrate, and the lattice constant, a. These morphological parameters are also those that one typically tries to extract during the inversion of experimental data sets using the BV model (more about this later). It should be noted that the BV model does not convey polarization coupling, and does not describe Rayleigh modes correctly; thus it is only an approximate solution for regular lattices. Indeed, the BV model was originally developed to treat the general problem of disordered particles on surfaces and the weak cross-polarized scattered signal was neglected. Moreover, the particle dimensions we will be concerned with, allow us to neglect both finite size and retardation effects in each particle (as is done in the BV model). We will in the following also neglect the plausible SiO_2 mound underneath each particle and treat the surface of the substrate as flat (i.e. as in Fig. 1(c)).

The open symbols in Figs. 4 and 5 represent the experimental normalized Mueller matrix elements $m_{12}(N)$, $m_{33}(C)$ and $m_{34}(S)$ for Samples A and B, respectively, as functions of photon energy for

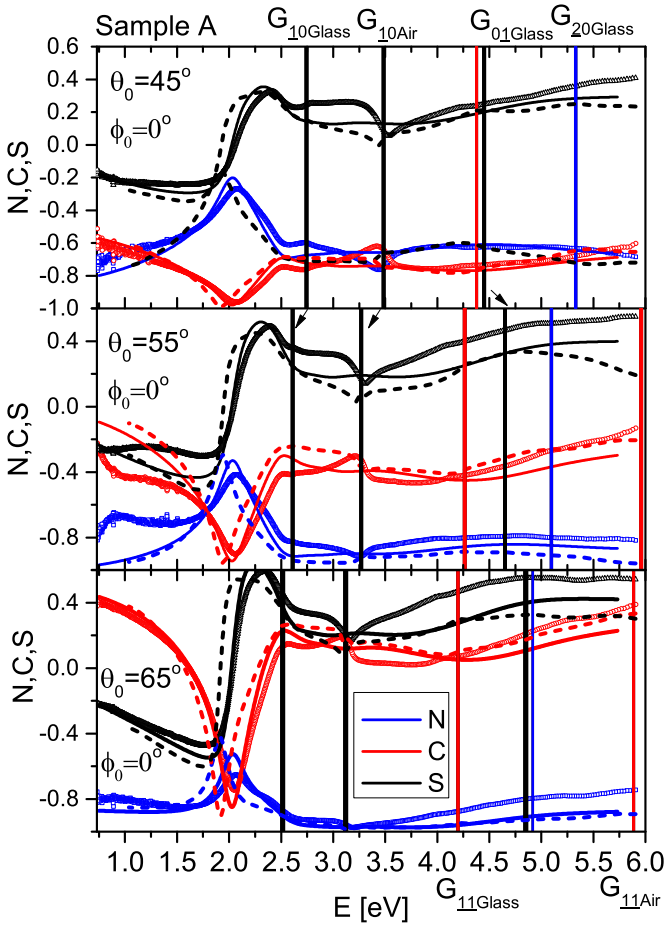

Fig. 4. The measured standard ellipsometric quantities $N = m_{21}$ (blue □); $C = m_{33}$ (red ○); and $S = m_{34}$ (black △) for Sample A as functions of photon energy for the three polar angles of incidence $\theta_0 = 45°$, 55° and 65° as indicated in each of the panels. The scattered signal was observed in the specular direction. The experimental data are shown as open symbols, and are selected for the azimuthal angle $\phi_0 = 0°$. The vertical lines indicate the photon energies of the corresponding Rayleigh lines. The results of the GranFilm simulations (the BV formalism) are shown as full lines, while the COMSOL simulations are given as dashed lines. The morphological parameters used in these simulations are given in Table 1; the GranFilm simulations assumed the parameter set corresponding to the smallest value of χ^2. (For interpretation of the references to color in this figure legend, the reader is referred to the web version of this article.)

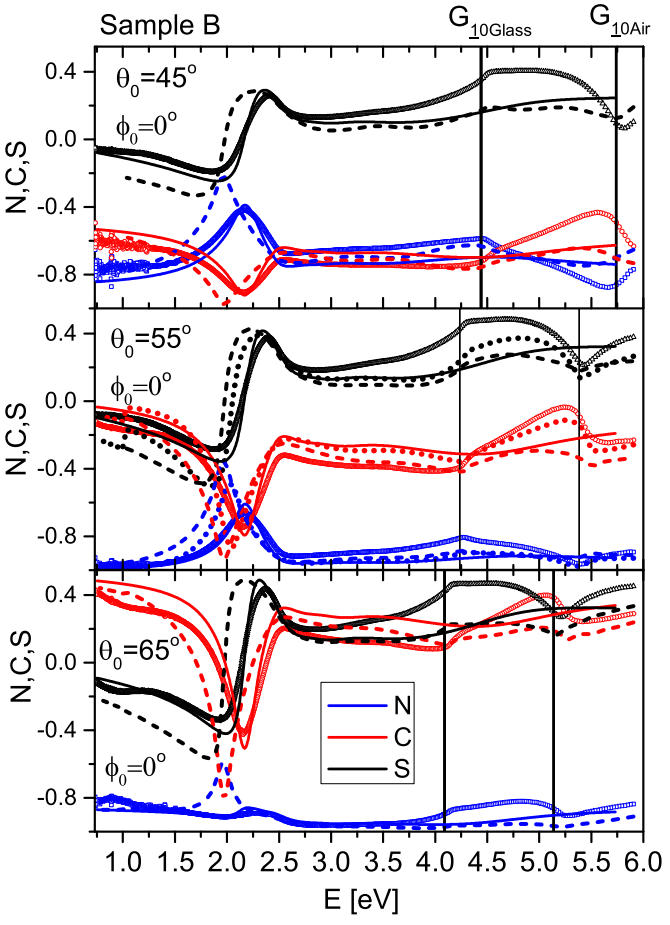

Fig. 5. Same as Fig. 4 but for Sample B. The COMSOL simulations used $(R_{xy}, R_z, a) = (38, 20, 125)$ nm (dashed lines), see Table 1. The GranFilm simulations assumed the parameter set corresponding to the smallest value of χ^2. The dotted lines shown in the middle panel for $\theta = 55°$ are COMSOL simulations with an added mound of height 20 nm, see Fig. 1(d).

the azimuthal angle of incidence $\phi_0 = 0°$ and three polar angles of incidence $\theta_0 = 45°$, 55° and 65°. The experimental data sets in Figs. 4 and 5 were then fitted with respect to the morphological parameters of the spheroidal lattice (R_{xy}, R_z and a) using the BV model as implemented in GranFilm [25]. The corresponding Mueller matrix elements obtained in this way are presented as full lines in Figs. 4 and 5 and the parameter sets that were obtained by this procedure are presented in Table 1. As can be observed from the values presented in Table 1, the morphological parameter obtained from SEM and AFM images (that are marked in boldface in Table 1) do not result in the smallest figure of merit, denoted χ^2 in the Table 1. For Sample A [Fig. 4] the lateral diameter of the particles $2R_{xy} = 116\,nm$ is at the limit of breakdown of the quasistatic approximation and some of the Rayleigh lines coincide with the position of the LSPR resulting in a perturbed signal around this photon energy. On the other hand, for Sample B a better agreement is found between the experimental morphological parameters and those resulting from a fitting procedure using the BV formalism, see Fig. 5; in this case the Rayleigh lines are shifted to higher energies and away from the LSPR, and the lateral particle size is smaller (than for Sample

Table 1
The morphology parameter sets (R_{xy}, R_z, a) (in nanometers) used in the numerical simulations performed using either GranFilm or COMSOL. The values that appear in boldface coincide with the values obtained from analyzing SEM and AFM images of the samples. It is noted that the values for R_z that were obtained from such images had considerable uncertainty associated with them. The GranFilm software was used for the purpose of reconstructing the morphology parameters of the samples by fitting the experimental data for the standard ellipsometric quantities presented in Figs. 4 and 5. This was done by defining a cost function that was minimized over parameter space using a mean square error estimator; the χ^2 values obtained in this way are reported. The star superscript ($\star$) indicates that the (COMSOL) simulation result corresponds to a geometry where the particles were on top of mounds of height 20 nm.

	GranFilm				COMSOL			
	R_{xy}	R_z	a	χ^2	R_{xy}	R_z	a	χ^2
Sample A	**58**	**30**	**210**	3.7	**58**	**30**	**210**	5.5
	60	29	198	2.6	–	–	–	–
Sample B	**34**	**20**	**125**	3.5	**34**	**20**	**125**	6.4
	34	29	114	2.1	**34**	**20***	**125**	3.0

A) so that the quasistatic approximation should be more accurate. However, as mentioned in Section 2, the manufactured samples did turn out to have some non-ideal characteristics, which probably will affect both the quality of the fit and the extracted morphological parameters that can be obtain from the BV approach. These aspects will be discussed in greater detail below.

It is worth noting that the BV model predicts that the optical response of a system consisting of a hemispheroidal island film supported by a planar substrate is *distinctly different* from that of an identical system but made with untruncated spheroidal particle (of the same volume) nearly touching the substrate [24,29,30]. Recently this latter system was studied by Mendoza-Galván et al. [26] who adapted the simplifying dipole approximation (known as the (modified) Yamaguchi model, see Refs. [15,31,32]). The advantage of considering untruncated particles, instead of truncated ones, in combination with the dipole approximation, is that one can easily obtain closed form expressions for the uniaxial effective medium dielectric functions [26].

3.3. Full wave simulations

The two structures, Sample A and Sample B, were also modelled using the Finite Element Method based commercial software package COMSOL Multiphysics, operating in the frequency-domain. The input to the simulations were the frequency dependent dielectric functions from the ellipsometric analysis of the deposited Au film, and SiO_2 data from the Woolam software database, in addition to the geometric parameters estimated from SEM and AFM, see Table 1. It is particularly interesting to use such a full wave tool in conjunction with real ellipsometric data, since the Finite Element Method has been regularly used for simulating the optical response of metamaterials, with consequent retrieval of effective optical parameters [8]. It is noted that this method can also be used to study modes, important in order to both interpret the optical response, but also in order to deduce bi-anisotropy and polarization coupling.

The simulations were performed using 4 ports with periodic Floquet boundary conditions to simulate the periodicity. The incident wave on port 1 was assumed either plane TE (s-polarized) or plane TM (p-polarized), along the $\mathbf{G}_{\parallel}^{(10)}$ direction. In the current work, the azimuthal angle was not changed.

The dashed lines in Figs. 4 and 5 present the standard ellipsometric quantities *N*, *C* and *S* calculated using COMSOL for both Samples A and B.

It is clear that the simulations to a large extent reproduce the block diagonal Mueller matrix, including the Rayleigh lines. This is evidently an important step in order to validate any EM simulator.

The simulations using the current model do not properly reproduce the experimental LSPR. As this problem occurs both in the BV and the COMSOL simulations, the models must be refined to include the SiO_2 mound as sketched in Fig. 1(d), which probably resulted from an over-etching during the FIB milling in between the Au particles. The dotted lines shown in the middle panel of Fig. 5 ($\theta_0 = 55^\circ$), was calculated using an additional 20 nm SiO_2 mound, as shown in Fig. 1(d). Indeed, the results show that the mound causes a blue shift of the LSPR, in addition to an improvement of the simulated response in the ultraviolet part of the spectrum. The simulation results that can be obtained using such refined models will be the topic for future work, among a full description of the polarization conversion.

In the simulations, both polarizations (TE and TM input) were run in parallel on a computer equipped with 32 GB RAM and an Intel i7-3930K processor operating at 3.2 GHz and running 64 bits Windows operating system. Typically, with an appropriate meshing, COMSOL used 1 minute per wavelength for Sample A and 13 seconds per wavelength for Sample B, with increasing computational time with added complexity (here the mound). Using a smaller number for the maximum allowed mesh size, considerably increases the computational time. It appears that for small unit cells and an optimized mesh size, fitting of ellipsometric data using finite element methods can in principle be performed on typical desk-top systems used in ellipsometric analysis. However, the required computational cost of such an approach will be orders of magnitude higher than when using GranFilm.

3.4. Direct Inversion (continuous film approximation)

It is common in the field ellipsometry to extract the effective optical properties of a thin film containing plasmonic nanoparticles. Therefore, we will below perform this analysis with the intention of comparing the results from such an approach to what can be obtained by other methods. A natural question then follows, what does an extracted dielectric function for an ultrathin layer represent? For such an ultrathin film (particles on the surface), and in view of the BV model, we learn that the resulting dielectric function is dependent on the substrate and thus not unique for the film. This behaviour is a direct consequence of the interaction between the particle and the substrate. A fitted effective dielectric function for the ultrathin effective film does not reveal the quantitative morphological parameters such as particle size/shape, density (lattice constant) and material, which is often sought in metrology. However, the effective dielectric function of this ultrathin layer may play an important role in terms of design and characterization of optical meta-surfaces, in particular with respect to controlling the propagation of surface bound waves, such as e.g. Surface Plasmon Polaritons on hyperbolic meta-surfaces [33].

The dielectric function of the effective film on the substrate was determined through a direct inversion of the Mueller matrix elements (principally sensitive to the *N*, *C*, and *S* quantities in Figs. 4 and 5). Fig. 6 shows the result of the inversion, where the dielectric tensor has been posed as an effective thin biaxial film. The film is as expected mainly uniaxial, but a small in-plane anisotropy was allowed for in order to reproduce some of the features observed in the off-diagonal elements of the Mueller matrix. The in-plane components were described by Bsplines where the initial guess was given by the fit of a Maxwell Garnett effective medium [1,34], while the out of plane component was simply described by a Bruggeman effective medium [1,34]. The thickness of the effective medium film was fixed to a "reasonable apriori-initial value" and not further fitted. The effective medium model is found to reproduce the data with high accuracy, and the fitted dielectric function gives indeed the position of the LSPR, and evidently it conveys non-quantitative information about particle-size and distribution (the distribution is evidently narrow in this idealized case), in addition to information about lattice interactions.

It is both interesting and instructive to establish a relationship between the BV formalism and the extracted dielectric function for the continuous effective film. To this end we start by neglecting the polarization coupling (in-plane anisotropy) and assume that the system has a uniaxial response. Under these assumptions, the relationship between the BV formalism and the effective medium film approach can be obtained by considering the first order Taylor expansion of the exponential function in the thin film formulas for a uniaxial film with the extraordinary axis perpendicular to the surface normal [28]. Let d be the thickness of the continuous thin film, and assume $d/\lambda \ll 1$, then

$$r_{012\nu} = \frac{r_{01\nu} + r_{12\nu}e^{-2iX_\nu}}{1 + r_{01\nu}r_{12\nu}e^{-2iX_\nu}} \approx \frac{r_{02\nu} - 2iX_\nu \frac{r_{12\nu}}{1+r_{01\nu}r_{01\nu}}}{1 - 2iX_\nu \frac{r_{01\nu}r_{12\nu}}{1+r_{01\nu}r_{12\nu}}}, \tag{8}$$

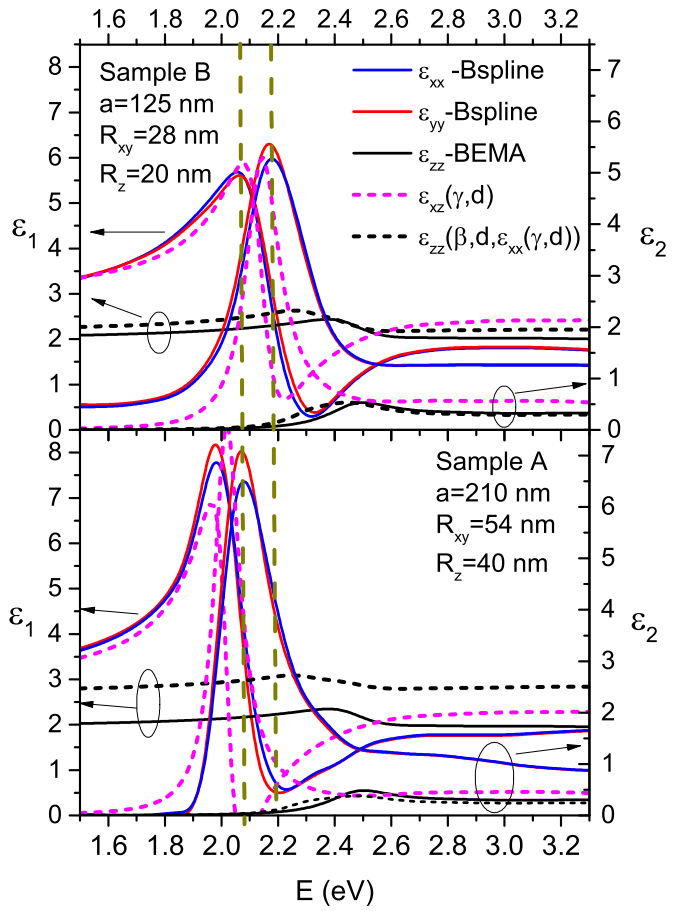

Fig. 6. Effective biaxial dielectric functions of Sample A (bottom Figure) and Sample B (top Figure). The biaxial Bspline inverted data are shown as full lines. The dielectric function calculated from γ and β (obtained from GranFilm) with the use of Eqs. (9) and (10) are shown as dashed lines. (For interpretation of the references to color in this figure legend, the reader is referred to the web version of this article.)

where $\nu = s, p$, and the expression for the Fresnel reflection amplitudes $r_{mn\nu}$ are given by Eqs. (4) and (6) after setting to zero the surface suceptibilities that appear in them; $\gamma = \beta = 0$ (see also Refs. [27,28]). In writing Eq. (8) we introduced the phase thickness (eigenmode) functions, X_ν, given in Azzam and Bashara [28].

To relate the reflection amplitudes in Eq. (8) to the reflection amplitudes obtained in the BV model, *e.g.*, Eqs. (5) and (7), we start by observing that the BV amplitude for s polarization depends only on the parallel susceptibility (γ), while the BV amplitude for p polarization depends both on the parallel and perpendicular susceptibilities (γ and β). Therefore, it is to be expected that the effective dielectric function $\varepsilon_{xx} = \varepsilon_{yy}$ will depend on γ but not β, in the same way as ε_{zz} will depend on β but not γ. In order to see if this assertion is true, we start by considering the case of s polarization. Equating the right hand side of Eq. (8) for $\nu = s$, with the corresponding BV formula in Eq. (5) gives the relationship:

$$\varepsilon_{xx} = \varepsilon_2 + \frac{\gamma}{d}, \tag{9}$$

where the thickness of the continuous thin film (d) must be chosen independently. Substituting the above expression for ε_{xx} into the right hand side of Eq. (8) for $\nu = p$, and equating the resulting expression with the corresponding BV formula, Eq. (7), results in

$$\frac{1}{\varepsilon_{zz}} = \frac{1}{\varepsilon_2} - \frac{\beta}{d}. \tag{10}$$

It is interesting to note that the effective medium dielectric functions add as disks on a substrate; additively parallel to the planar surface and capacitively perpendicular to it.

The fitted uniaxial dielectric function extracted from the ellipsometric data can now in principle be related to morphological parameters through the BV formalism as is the case for an effective medium theory. Using the calculated γ and β from the BV model implemented in GranFilm, and the relationship in Eqs. (9) and (10), we finally obtain the uniaxial dielectric function plotted (dashed lines) in Fig. 6. In both cases, the parameter d is adjusted to make a reasonable fit (we used $d = 1.0\,nm$ for Sample B and $d = 1.9\,nm$ for Sample A, but it is emphasized that these values depend on the initial choice for the thickness in the direct inversion).

The dielectric function calculated based on Eqs. (9) and (10) turns out to be in reasonable agreement with the one obtained by inversion (see Fig. 6). The difference is in particular, a small red-shift of the one calculated from the BV formalism, and the more asymmetric shape towards higher energies of the Bspline inverted one. The correspondence appears better for Sample B, as expected. This red-shift was also observed from the COMSOL simulations, and was probably a result of reduced screening by the substrate, again as a result of the over-etching of the substrate (i.e. the particles are sitting on a small SiO_2 mound). The real part of the calculated ε_z component is observed to be off-set from the inverted one. Indeed, it is difficult to invert for the z-component accurately using ellipsometry, and it is strongly correlated to the chosen film thickness. As a result, in future work, it appears better to replace the initial guess by the dielectric function produced by GranFilm.

4. Conclusions

Mueller Matrix Ellipsometry reveals a complex optical response from a simple square array of Au-nanoparticles supported by a glass substrate. In particular, polarization conversion is found around the Localized Surface Plasmon Resonance (LSPR), and along Rayleigh lines. The Rayleigh lines can be used to find the orientation of the sample, and through a simple second order equation be used to directly estimate lattice constants.

It is found that for a regular 2D lattice, the Bedaux-Vlieger formalism can extract reasonable parameters related to particle dimensions, as long as the Rayleigh anomalies are well above the LSPR. However, the weak polarization conversion around the plasmon resonance and the small dispersion of the plasmon resonance with respect to the azimuthal rotation of the substrate cannot be modelled within the current formulation of the latter formalism.

The finite element method appears, when using periodic boundary conditions, to reasonably well model the ellipsometric spectra including the Rayleigh lines.

Both methods show that imperfections in the system, such as a dielectric mound, must be included in the model in order to reproduce well the recorded data. The Bedaux-Vlieger formalism must be reworked in order to include such an over-etching into the substrate, while it can be easily added to the Finite Element model.

The GranFilm implementation of the Bedeaux-Vlieger model is computationally fast (spectra calculated in fraction of seconds), in addition to being highly instructive. The Finite Element Model appears much more versatile and seems accurate, but is computationally expensive (spectra calculated in 30 minutes to several hours, depending on number of spectral points, meshing and unit cell size).

The substrate dependent effective uniaxial dielectric function for an equivalent continuous ultra-thin film was extracted by direct inversion of the ellipsometric data. It is possibly to give a meaning to this dielectric function by e.g. correlating it to the one directly estimated in the continuous film limit of the Bedaux-Vlieger

formalism. It is envisaged that the latter dielectric function may be useful in the description of meta-surfaces, therein e.g. to estimate the propagation of surface waves.

Acknowledgements

The research of I.S. was supported in part by the Research Council of Norway, Contract No. 216699, and The French National Research Agency (ANR) under grant ANR-15-CHIN-0003-01.

References

[1] T. Oates, H. Wormeester, H. Arwin, Characterization of plasmonic effects in thin films and metamaterials using spectroscopic ellipsometry, Prog. Surf. Sci. 86 (2011) 328–376.
[2] T. Brakstad, M. Kildemo, Z. Ghadyani, I. Simonsen, Dispersion of polarization coupling, localized and collective plasmon modes in a metallic photonic crystal mapped by Mueller matrix ellipsometry, Opt. Express 23 (2015) 22800–22815.
[3] F. Monticone, A. Alù, Metamaterials and plasmonics: from nanoparticles to nanoantenna arrays, metasurfaces, and metamaterials, Chin. Phys. B 23 (2014) 047809.
[4] S. Maier, Plasmonics: Fundamentals and Applications, Springer, New York, 2007.
[5] N.G. Khlebtsov, L.A. Dykman, Optical properties and biomedical applications of plasmonic nanoparticles, J. Quant. Spectrosc. Radiat. Transf. 111 (2010) 1–35.
[6] R.A. Shelby, D.R. Smith, S. Schultz, Experimental verification of a negative index of refraction, Science 292 (2001) 77–79.
[7] N. Fang, H. Lee, C. Sun, X. Zhang, Subdiffraction-limited optical imaging with a silver superlens, Science 308 (2005) 534–537.
[8] D.R. Smith, S. Schultz, P. Markoš, C.M. Soukoulis, Determination of effective permittivity and permeability of metamaterials from reflection and transmission coefficients, Phys. Rev. B 65 (2002) 195104.
[9] L.M.S. Aas, M. Kildemo, C. Martella, M.C. Giordano, D. Chiappe, F.B. de Mongeot, Optical properties of biaxial nanopatterned gold plasmonic nanowired gridpolarizer, Opt. Express 21 (2013) 30918–30931.
[10] T.W.H. Oates, M. Ranjan, S. Facsko, H. Arwin, Highly anisotropic effective dielectric functions of silver nanoparticle arrays., Opt. Express 19 (2011) 2014–2028.
[11] M. Ranjan, T.W.H. Oates, S. Facsko, W. Möller, Optical properties of silver nanowire arrays with 35 nm periodicity, Opt. Lett. 35 (2010) 2576–2578.
[12] N. Guth, B. Gallas, J. Rivory, J. Grand, A. Ourir, G. Guida, R. Abdeddaim, C. Jouvaud, J. de Rosny, Optical properties of metamaterials: influence of electric multipoles, magnetoelectric coupling, and spatial dispersion, Phys. Rev. B 85 (2012) 115138.
[13] D. Schmidt, B. Booso, T. Hofmann, E. Schubert, A. Sarangan, M. Schubert, Generalized ellipsometry for monoclinic absorbing materials: determination of optical constants of cr columnar thin films, Opt. Lett. 34 (2009) 992–994.
[14] G.K. Larsen, Y. Zhao, Extracting the anisotropic optical parameters of chiral plasmonic nanostructured thin films using generalized ellipsometry, Appl. Phys. Lett. 105 (2014) 071109.
[15] D. Bedeaux, J. Vlieger, Optical Properties Of Surfaces, 2nd Ed., Imperial College Press, London, 2004.
[16] I. Simonsen, Optics of surface disordered systems: a random walk through rough surface scattering phenomena, Eur. Phys. J. Spec. Top. 181 (2010) 1–103.
[17] T. Nordam, P. Letnes, I. Simonsen, Numerical simulations of scattering of light from two-dimensional surfaces using the reduced Rayleigh equation, Front. Phys. 1 (2013) 8.
[18] J.-P. Banon, M. Kildemo, I. Simonsen, Accurate Metrology of Arrays of Rounded Plasmonic Particles Using Reduced Rayliegh Equations and Mueller Matrix Ellipsometry, 2017, unpublished.
[19] Lord Rayleigh, On the dynamical theory of gratings, Proc. R. Soc. (Lond.) Ser. A 79 (1907) 399–416.
[20] L.M.S. Aas, M. Kildemo, Y. Cohin, E. Søndergård, Determination of small tilt angles of short gasb nanopillars using UV–visible Mueller matrix ellipsometry, Thin Solid Films 541 (2012) 97–101.
[21] Z. Ghadyani, M. Kildemo, L.M.S. Aas, Y. Cohin, E. Søndergård, Anisotropic plasmonic Cu nanoparticles in sol–gel oxide nanopillars studied by spectroscopic Mueller matrix ellipsometry, Opt. Express 21 (2013) 30796–30811.
[22] C. Menzel, T. Paul, C. Rockstuhl, T. Pertsch, S. Tretyakov, F. Lederer, Validity of effective material parameters for optical fishnet metamaterials, Phys. Rev. B 81 (2010) 035320.
[23] I. Simonsen, R. Lazzari, J. Jupille, S. Roux, Numerical modeling of the optical response of supported metallic particles, Phys. Rev. B 61 (2000) 7722–7733.
[24] R. Lazzari, I. Simonsen, D. Bedeaux, J. Vlieger, J. Jupille, Polarizability of truncated spheroidal particles supported by a substrate: model and applications, Eur. Phys. J. B 24 (2001) 267–284.
[25] R. Lazzari, I. Simonsen, GranFilm: a software for calculating thin-layer dielectric properties and Fresnel coefficients, Thin Solid Films 419 (2002) 124–136.
[26] A. Mendoza-Galván, K. Järrendahl, A. Dmitriev, T. Pakizeh, M. Käll, H. Arwin, Optical response of supported gold nanodisks, Opt. Express 19 (2011) 12093–12107.
[27] J. Jackson, Classical Electrodynamics, 3rd Ed., John Wiley & Sons, New York, 2007.
[28] R.M.A. Azzam, N.M. Bashara, Ellipsometry and Polarized Light, North-Holland Publishing Company, Amsterdam, 1977.
[29] R. Ruppin, Surface modes and optical absorption of a small sphere above a substrate, Surf. Sci. 127 (1983) 108–118.
[30] R. Lazzari, S. Roux, I. Simonsen, J. Jupille, B. Bedeaux, V. Vlieger, Multipolar plasmon resonances in supported silver particles: the case of Ag/α-Al_2O_3(0001), Phys. Rev. B 65 (2002) 235424.
[31] T. Yamaguchi, S. Yoshida, A. Kinbara, Optical effect of the substrate on the anomalous absorption of aggregated silver films, Thin Solid Films 21 (1974) 173–187.
[32] V.A. Fedotov, V.I. Emel'yanov, K.F. MacDonald, N.I. Zheludev, Optical properties of closely packed nanoparticle films: spheroids and nanoshells, J. Opt. A, Pure Appl. Opt. 6 (2004) 155–160.
[33] J.S. Gomez-Diaz, M. Tymchenko, A. Alù, Hyperbolic metasurfaces: surface plasmons, light-matter interactions, and physical implementation using graphene strips, Opt. Mater. Express 5 (2015) 2313–2329.
[34] G.A. Niklasson, C.G. Granqvist, O. Hunderi, Effective medium models for the optical properties of inhomogeneous materials, Appl. Opt. 20 (1981) 26–30.